



Data assimilation strategies for volcano geodesy



Yan Zhan ^{*}, Patricia M. Gregg

Department of Geology, University of Illinois – Urbana-Champaign, Natural History Building, 1301 W Green St., Urbana, IL 61801, United States

ARTICLE INFO

Article history:

Received 23 July 2016

Received in revised form 23 January 2017

Accepted 18 February 2017

Available online 24 February 2017

Keywords:

Volcanic unrest

Ensemble Kalman filter

GPS

InSAR

Geodynamic models

ABSTRACT

Ground deformation observed using near-real time geodetic methods, such as InSAR and GPS, can provide critical information about the evolution of a magma chamber prior to volcanic eruption. Rapid advancement in numerical modeling capabilities has resulted in a number of finite element models targeted at better understanding the connection between surface uplift associated with magma chamber pressurization and the potential for volcanic eruption. Robust model-data fusion techniques are necessary to take full advantage of the numerical models and the volcano monitoring observations currently available. In this study, we develop a 3D data assimilation framework using the Ensemble Kalman Filter (EnKF) approach in order to combine geodetic observations of surface deformation with geodynamic models to investigate volcanic unrest. The EnKF sequential assimilation method utilizes disparate data sets as they become available to update geodynamic models of magma reservoir evolution. While the EnKF has been widely applied in hydrologic and climate modeling, the adaptation for volcano monitoring is in its initial stages. As such, our investigation focuses on conducting a series of sensitivity tests to optimize the EnKF for volcano applications and on developing specific strategies for assimilation of geodetic data. Our numerical experiments illustrate that the EnKF is able to adapt well to the spatial limitations posed by GPS data and the temporal limitations of InSAR, and that specific strategies can be adopted to enhance EnKF performance to improve model forecasts. Specifically, our numerical experiments indicate that: (1) incorporating additional iterations of the EnKF analysis step is more efficient than increasing the number of ensemble members; (2) the accuracy of the EnKF results are not affected by initial parameter assumptions; (3) GPS observations near the center of uplift improve the quality of model forecasts; (4) occasionally shifting continuous GPS stations to provide variability in the locations of observations results in better model predictions than utilizing fixed locations when the number of available instruments is limited; (5) spotty InSAR data coverage on the flanks of a volcano due to topographic shadows and/or atmospheric interference does not adversely impact the effectiveness of EnKF if the available coverage is >50%; and (6) snow or glacial obstruction in the center of uplift can adversely impact EnKF forecasts. By utilizing these strategies, we conclude that the EnKF is an effective sequential model-data fusion technique for assimilating multiple geodetic observations to forecast volcanic activity at restless volcanoes.

© 2017 Elsevier B.V. All rights reserved.

1. Introduction

Assessing the unrest of volcanic systems around the world requires a multi-disciplinary approach that utilizes disparate datasets to analyze volcano observations. Over the past decades, significant effort has been expended to develop monitoring strategies to mitigate potential disasters for vulnerable populations living in the shadows of active volcanoes. Geodetic monitoring methods, including Global Positioning System (GPS) (e.g. Beauducel and Cornet, 1999; Bevis and Foster, 2000; Bonforte and Puglisi, 2003, 2006; Rivet et al., 2014) and Interferometric Synthetic Aperture Radar (InSAR) (Massonnet and Feigl, 1998; Sigmundsson et al., 1999; Lu et al., 2000; Chaussard et al., 2013; Papoutsis et al., 2013; Pinel et al., 2014; Le Mével et al., 2015; Morales Rivera et al., 2015; Masterlark et al., 2016a), provide 4D surface

deformation observations of volcanoes experiencing unrest, and give insight into the dynamic evolution of the magma systems below. Advancements in geodetic data collection and analysis have shown the capability to detect volcano inflation and provide early warning of volcanic unrest sometimes years in advance of measurable seismicity (Lu et al., 2010; Chaussard and Amelung, 2012; Chaussard et al., 2013; Biggs et al., 2014).

To analyze surface deformation observations, classic inversion and joint inversion strategies have been developed using analytical solutions such as the elastic Mogi (1958) model and its derivatives (McTigue, 1987; Massonnet and Feigl, 1998; Battaglia et al., 2003a, 2003b; Nooner and Chadwick, 2009; Newman et al., 2012; Parks et al., 2015). To adapt static analytical approximations of volcano evolution into time-forward models, the evolution of static models can be solved as a function of time (Newman et al., 2006). Alternatively, time-dependent kinematic models can be used in a model-data fusion framework to provide the temporal variation (Desmarais and Segall, 2007; Anderson and Segall,

^{*} Corresponding author.

E-mail address: yanzhan3@illinois.edu (Y. Zhan).

2013). The strength of analytical and kinematic solutions is that they provide first order solutions with relative computational ease. However, they are limited in their ability to solve complex multiphysics problems.

Thermomechanical numerical models offer an additional means to decipher observations of deformation and investigate precursory signals for eruptions (e.g. Currenti et al., 2007; Gregg et al., 2012, 2013; Ronchin et al., 2013; Cannavò et al., 2015), and may be used to invert geodetic observations through optimization schemes (Carbone et al., 2007; Hickey et al., 2013). The integration of geodetic measurements into multiphysics dynamic models has been shown to provide advanced understanding of how highly non-linear volcano systems evolve in time (Cianetti et al., 2012; Gregg et al., 2013; Alparone et al., 2013; Hickey et al., 2015). While these inversion approaches work well for combining one or potentially two data streams with numerical models, they are static assessments of the system state and do not provide updates or forecasts. Unlike their kinematic modeling counterparts (e.g., Anderson and Segall, 2013), robust time-sequential data assimilation strategies that link sophisticated numerical models with observations have not been widely used in volcano studies and must be developed to fully realize the potential of numerical modeling approaches.

To work towards the goal of a multi-data stream forecasting method for volcanic application, Gregg and Pettijohn (2016) developed a 2D data assimilation framework based on the Ensemble Kalman Filter (EnKF) method (Fig. 1). Widely applied in hydrologic, physical oceanography, and climate modeling (vanLeeuwen and Evensen, 1996; Allen et al., 2003; Bertino et al., 2003; Brusdal et al., 2003; Natvik and Evensen, 2003; Lisaeter et al., 2007; Skjervheim et al., 2007; Evensen, 2009a, 2009b; Seiler et al., 2010; Wilson et al., 2010; Wilson and Özkan-Haller, 2012; Wilson et al., 2014), the EnKF has been shown to be a powerful forecasting tool for assimilating highly disparate observations into complex dynamic models. The EnKF method has proven to be a more efficient and computationally economical approach than the traditional Kalman Filter (Kalman, 1960) and the Extended Kalman Filter (Schmidt, 1966) because the covariance matrix in the EnKF analysis is estimated using a Markov Chain Monte Carlo (MCMC) approach

allowing for updates of both the model state and model parameters concurrently (Evensen, 2003, 2009a). The MCMC approach utilized by the EnKF has a proven track record (Evensen, 2003, 2009a) for performing well with highly nonlinear systems where the traditional Kalman Filter and pseudo non-linear Extended Kalman Filter may perform suboptimally (Julier et al., 2000). Furthermore, the ensemble based method enables users to swap in model advancements without making major adjustments to the data assimilation procedure (Evensen, 2003, 2009a). By assimilating surface deformation data, the EnKF is able to swiftly update the parameters for the magma reservoir by matching new measurements with the numerical model forecasting (Gregg and Pettijohn, 2016).

Although this study focuses on utilizing synthetic data to explore the usage of the Ensemble Kalman Filter in volcanology, it offers several critical advancements over the implementation of Gregg and Pettijohn (2016). First, we establish a new 3-dimensional EnKF framework, which significantly expands the use of this data assimilation method in volcanology. The ability to assimilate data into a 3D models is critical for analyzing the inherent 3D nature of volcanic systems, such as asymmetric magma reservoirs, topography, faults, and host rock heterogeneities (e.g. Cannavò et al., 2015; Hickey et al., 2015). Second, this study introduces an important improvement in the EnKF algorithm itself. As an enhancement to the traditional EnKF framework (Evensen, 2003, 2009a; Gregg and Pettijohn, 2016), we develop and apply an iterative EnKF algorithm, which, as we illustrate, is more effective in highly non-linear problems such as volcanic unrest. Third, instead of using idealized synthetic data (Gregg and Pettijohn, 2016), we add synthetic noise to both synthetic GPS and InSAR signals. Testing more realistic error models (e.g. Mao et al., 1999; Williams et al., 2004; Lohman and Simons, 2005; Fattahi and Amelung, 2015) allows us optimize the EnKF analysis more wisely, test whether this strategy will be able to effectively analyze real data in the future. Fourth, in addition to utilizing more realistic noise models to mimic real data errors, we also simulate defects which are inevitable in real measurements such as gaps in data coverage and continuity. These tests not only provide information

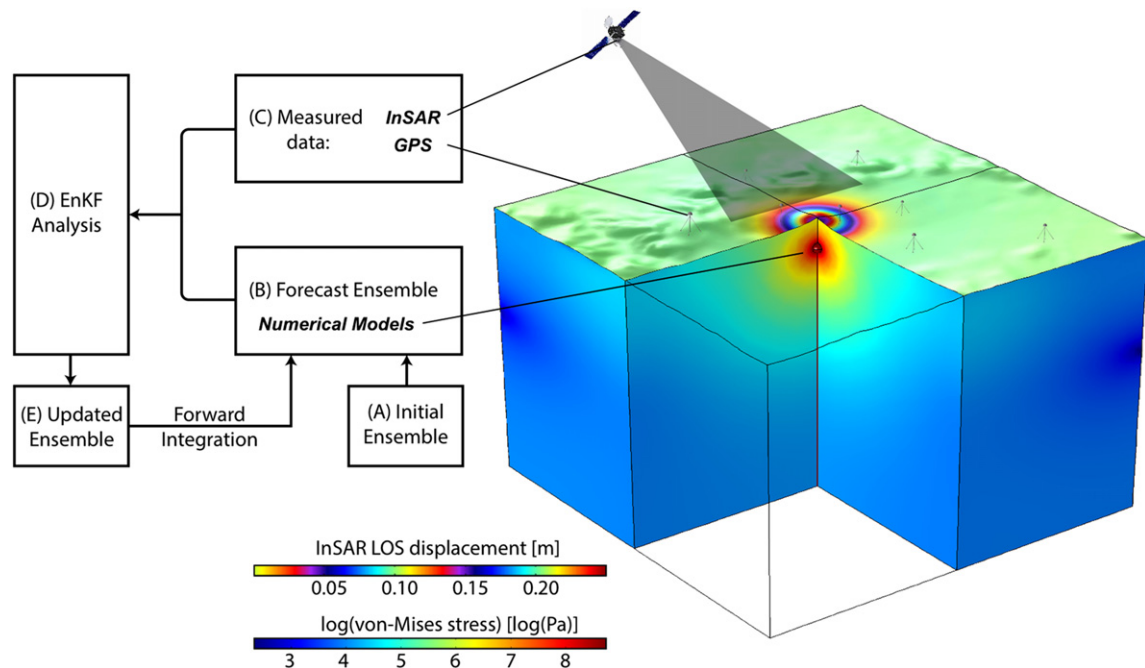


Fig. 1. Illustration of the data assimilation strategy for magma reservoir modeling. The example model shows the predicted surface deformation (top surface) and von Mises stress (at depth) due to a magma chamber volume change of 0.003 km^3 . The Ensemble Kalman Filter (EnKF) approach is modified from Gregg and Pettijohn (2016). (A) The initial ensemble of models is produced, including model uncertainties. The forecast ensemble (B) is sequentially derived from forward integration of the initial suite of models. (C) Data utilized in this implementation include InSAR and/or GPS, but could also include additional such as gravity, seismicity, and tomography. (D) When new data are available, an EnKF analysis is conducted to update the model parameters (E) and change the trajectory of the model. The updated model parameters are then used to create a new forecast ensemble.

for using the EnKF analysis to enhance our modeling techniques, but also give insights into data collection optimization. Finally, this study conducts systematic sensitivity tests to exam the EnKF analysis results affected by prescribed model setup conditions such as the number of ensemble members, the number of iterations, and the initial guess of model parameters in order to improve the EnKF performance while minimizing computational costs.

2. Methods

2.1. Magma reservoir finite element model

We use a 3D viscoelastic finite element model (FEM) to create a time series of surface deformation to provide synthetic GPS and InSAR datasets for the data assimilation. The numerical approach was modified after previous 2D and 3D finite element models for magma reservoirs (Grosfils, 2007; Del Negro et al., 2009; Gregg et al., 2012, 2013; Gregg and Pettijohn, 2015; Grosfils et al., 2015). The crust surrounding a magma reservoir is simulated by a box with a spherical void, which is loaded from within to create an inflating volume change, ΔV (Fig. 2). The size of the box is 60 km \times 60 km \times 20 km, consistent with the common scale of terrestrial volcanic systems (Gregg and Pettijohn, 2016). The sides and bottom of the box are defined by roller boundary conditions. A constant gravity ($g = 9.8 \text{ m/s}^2$) and an initial isostatic stress are balanced to maintain the lithostatic state of the system (Fig. 2b):

$$\sigma_1^{\text{initial}} = \sigma_2^{\text{initial}} = \sigma_3^{\text{initial}} = \rho g z \quad (1)$$

where $\sigma_k^{\text{initial}}$ is the initial principle stress, z is the depth, and $\rho = 2700 \text{ kg/m}^3$ is the density of the host rocks.

COMSOL Multiphysics 5.1® is utilized to calculate the model mesh. The mesh grids are coarse within the outer domain far away from the volcano and refined in the inner box close to the center of the magma chamber (Fig. 2a). We apply a linear viscoelastic stress-strain relation with Maxwell model to calculate stress and strain resulting from an applied load, following:

$$\dot{\epsilon} \propto \frac{\sigma}{\eta} + \frac{\dot{\sigma}}{G} \quad (2)$$

where $\dot{\epsilon}$ is strain rate, σ is stress, $\dot{\sigma}$ is stress rate, η and G are constants. The viscosity η is defined as $2 \times 10^{16} \text{ Pa}\cdot\text{s}$ and the shear modulus is defined by $G = E/2(1 + \nu)$, where the Young's modulus E is 75 GPa and Poisson ratio ν is 0.25. The material properties are defined to simulate synthetic terrestrial volcano. However, future data assimilation efforts on natural systems will allow for estimating variations in material properties from geophysical observations such as tomography.

The predicted surface deformation from the 3D numerical approach is consistent with the viscoelastic analytical solution of Gregg et al. (2012) modified from Del Negro et al. (2009) (Fig. 3). The volume changes ΔV , due to the expansion of the magma reservoir, is defined as a function of time (Fig. 2b). During the first and the third year, continuous inflation mimics possible magma injection. The inflation ceases in the second year approximating a volcanically silent period between injections (Table 1).

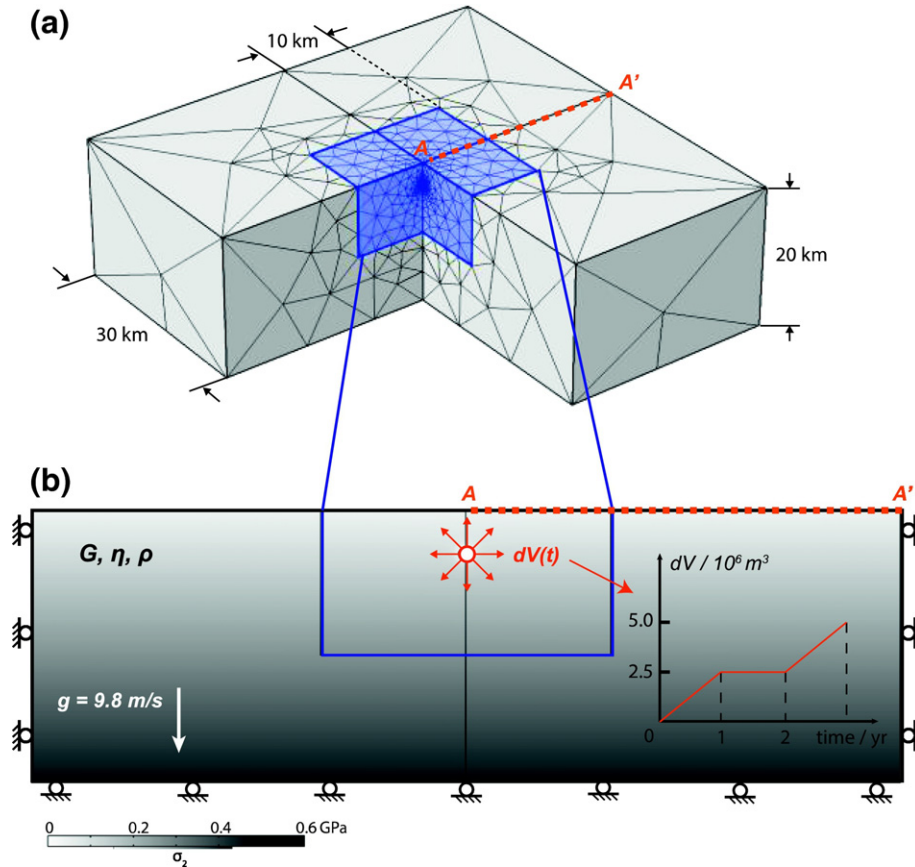


Fig. 2. Finite Element Model (FEM) setup used to produce the synthetic InSAR and GPS data sets. (a) The 3D model is finely meshed near the magma reservoir and coarsens at distance away from the center of the expanding magma chamber. (b) The boundary conditions of the model follow Gregg et al. (2012) and are adapted for the 3D implementation. Roller, zero normal displacement, conditions are applied on the sides and bottom of the model, a free surface is assumed at the top of the model, and a pressure boundary condition is applied along the magma chamber to produce the volume change shown in the inset. The grey scale illustrates the magnitude of the isostatic stress due to gravitational loading. The line AA' is used for the displacements benchmark provided in Fig. 3.

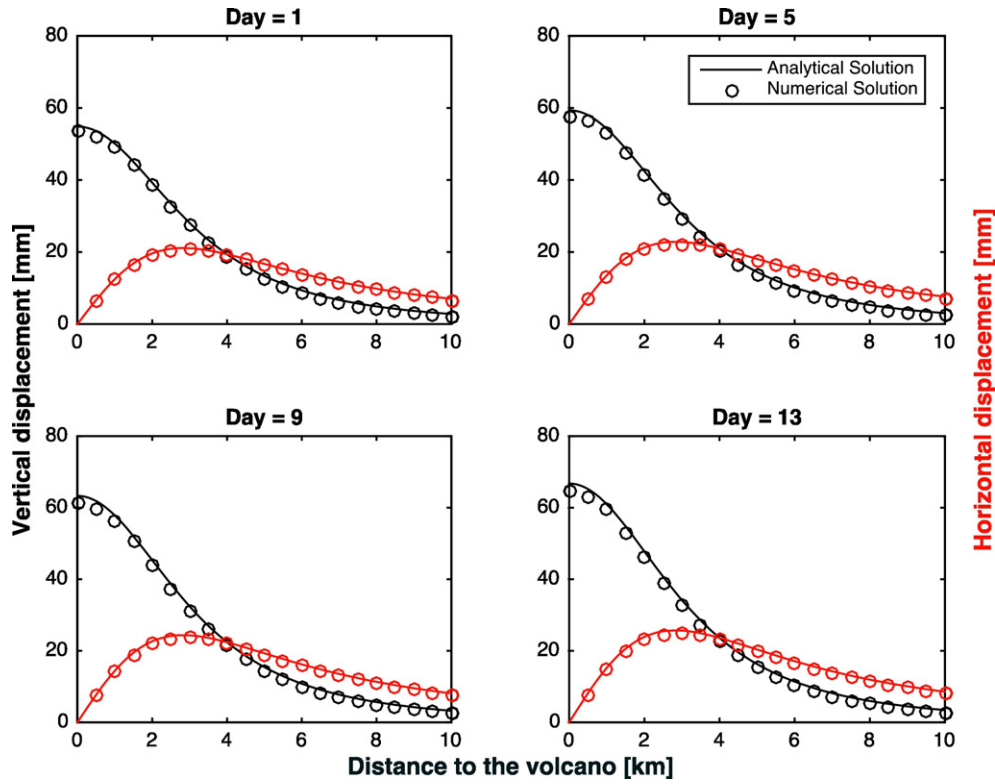


Fig. 3. Benchmarks for surface displacement predicted by the 3D model. Vertical motion is shown in black and horizontal motion in red. We compare the 3D viscoelastic numerical solution provided by COMSOL, solid lines, with the viscoelastic analytical solution, circles (Eq. (1); Gregg et al., 2012).

2.2. Synthetic data

The synthetic data created by the FEM described in Section 2.1 are utilized to systematically investigate the performance of the EnKF. The synthetic datasets, including single component line of sight (LOS) “InSAR”, and multi-component “GPS”, are calculated based on defined parameters (Table 2), which the EnKF analysis attempts to find.

Table 1
Notations.

Symbol	Description
\mathbf{A}	Forecast ensemble matrix
\mathbf{A}'	Ensemble perturbation matrix
\mathbf{A}^a	EnKF analysis matrix
\mathbf{P}_e	Covariance matrix for model perturbation
\mathbf{R}_e	Covariance matrix for measurement perturbation
\mathbf{D}	Measurement matrix
$\delta\mathbf{d}$	Measurement perturbation matrix
\mathbf{H}	Mapping matrix
Γ_p	Parameter space tolerance
N_{ens}	Number of ensembles
N_{par}	Number of parameters
N_{mes}	Number of measurements
N_{dim}	Number of parameters adding with measurements
Z_i^a	Assumed parameter (i) for synthetic
Z_i^a	EnKF updated parameter (i)
t	Time
dP	Source overpressure
dV	Source volume change
ν	Poisson ratio
E	Young's modulus
G	Shear modulus
$\dot{\epsilon}$	Strain rate
$\dot{\sigma}$	Stress rate
η	Viscosity
ρ	Density
σ	Stress

The synthetic InSAR LOS data are created by calculating the surface deformation difference between two sequential time steps, collected every 60 days in a 10 km × 10 km grid with a lateral resolution of 20 m. All the synthetic LOS data are composed of both signal and noise (Fig. 4a). We followed Lohman and Simons (2005) to create synthetic distance-correlated noise, \mathbf{n}_c , which exhibits a power law behavior mainly correlated to atmospheric structures (Agram and Simons, 2015; Fattahi and Amelung, 2015). The distance-correlated noise, \mathbf{n}_c is derived from a predetermined covariance matrix, \mathbf{C}_d (Lohman and Simons, 2005):

$$C_d^{ij} = e^{-L^{ij}/L_c} \quad (3)$$

$$\mathbf{n}_c = \mathcal{L} \times \mathbf{n}_n \quad (4)$$

where L^{ij} is distance between the i th and j th points, and L_c is the window size. \mathcal{L} is the lower triangular matrix derived from \mathbf{C}_d by Cholesky decomposition, and \mathbf{n}_n is the uncorrelated noise matrix. Although many previous studies revealed that other factors like topography also contribute to the LOS delay (e.g. Jónsson et al., 2002; Emardson et al., 2003), we neglect those effects and only consider a spatially stationary and isotropic noise model, since the purpose of this paper is discussing the performance of the Ensemble Kalman Filter.

Applying the full “InSAR” dataset is prohibitively computationally expensive as full resolution interferograms contain more than one million points. Therefore, we reduce the InSAR sampling points from $\sim 10^6$ to ~ 800 (Fig. 4d), through a root-mean-square-error (RMSE) based quadtree algorithm (e.g., Jónsson et al., 2002).

The synthetic GPS observations are collected every day at 20 synthetic GPS stations whose locations are shown in the Fig. S1. The “GPS” data are composed of three components east-west, north-south, and up-down. The three components are directly interpolated from the finite element model output. In addition, we add noise to the signal to create a more realistic synthetic GPS data. We utilize a combination of

Table 2
Parameters used for the synthetic model.

Parameter	Value
Chamber location in X (m)	0
Chamber location in Y (m)	0
Chamber depth (m)	3000
Chamber radius (m)	500
Maximum volume change (km ³)	0.005

white and flicker noise model (e.g. Zhang et al., 1997; Mao et al., 1999; Williams et al., 2004; Dmitrieva et al., 2015) as the uncertainty of the “GPS” data. Since the uncertainty of the up-down component is obvious higher than other two components (Mao et al., 1999), we assume 1 mm/yr of uncertainty in the horizontal components and 5 mm/yr in vertical one (Fig. 4c). Before the synthetic data are utilized in EnKF analysis, the full signal, with noise, is smoothed by a low pass filter (Fig. 4c).

2.3. Ensemble Kalman filter

The Ensemble Kalman Filter (EnKF) is a data assimilation method built upon the traditional Kalman Filter (KF) approach (Kalman, 1960). The EnKF utilizes a Markov chain of Monte Carlo (MCMC)

method to solve the time evolution of the probability density function of the model. This update overcomes the limitations of the Kalman Filter and Extended Kalman Filter methods, such as computational expensive, storage issues, and poor performance with highly nonlinear problems (Evensen, 2009a, 2009b). We follow the EnKF analysis scheme described by Evensen (2003) and Gregg and Pettijohn (2016) (Fig. 1), which we briefly describe below.

The forecast ensemble members $\psi_i \in \mathbb{R}^{Ndim}$, composed by both parameters and solutions, are stored in

$$\mathbf{A} = (\psi_1, \psi_2, \dots, \psi_{Nens}) \in \mathbb{R}^{Ndim \times Nens} \quad (5)$$

where $Ndim$ is the number of the parameters and measurements and $Nens$ is the number of ensemble members. In the first step, the initial ensemble members are calculated based on an initial guess of the model parameters. For the magma reservoir models in this study, unknown parameters include the geometry, location, and volume change, while the rheological properties of the host rock are assumed. Thus, an initial parameter space is built by Monte Carlo methods to derive the initial solution space according to the equation of the Mogi (1958) model.

The ensemble perturbation matrix is defined as

$$\mathbf{A}' = \mathbf{A}(\mathbf{I} - \mathbf{1}_{Nens}) \quad (6)$$

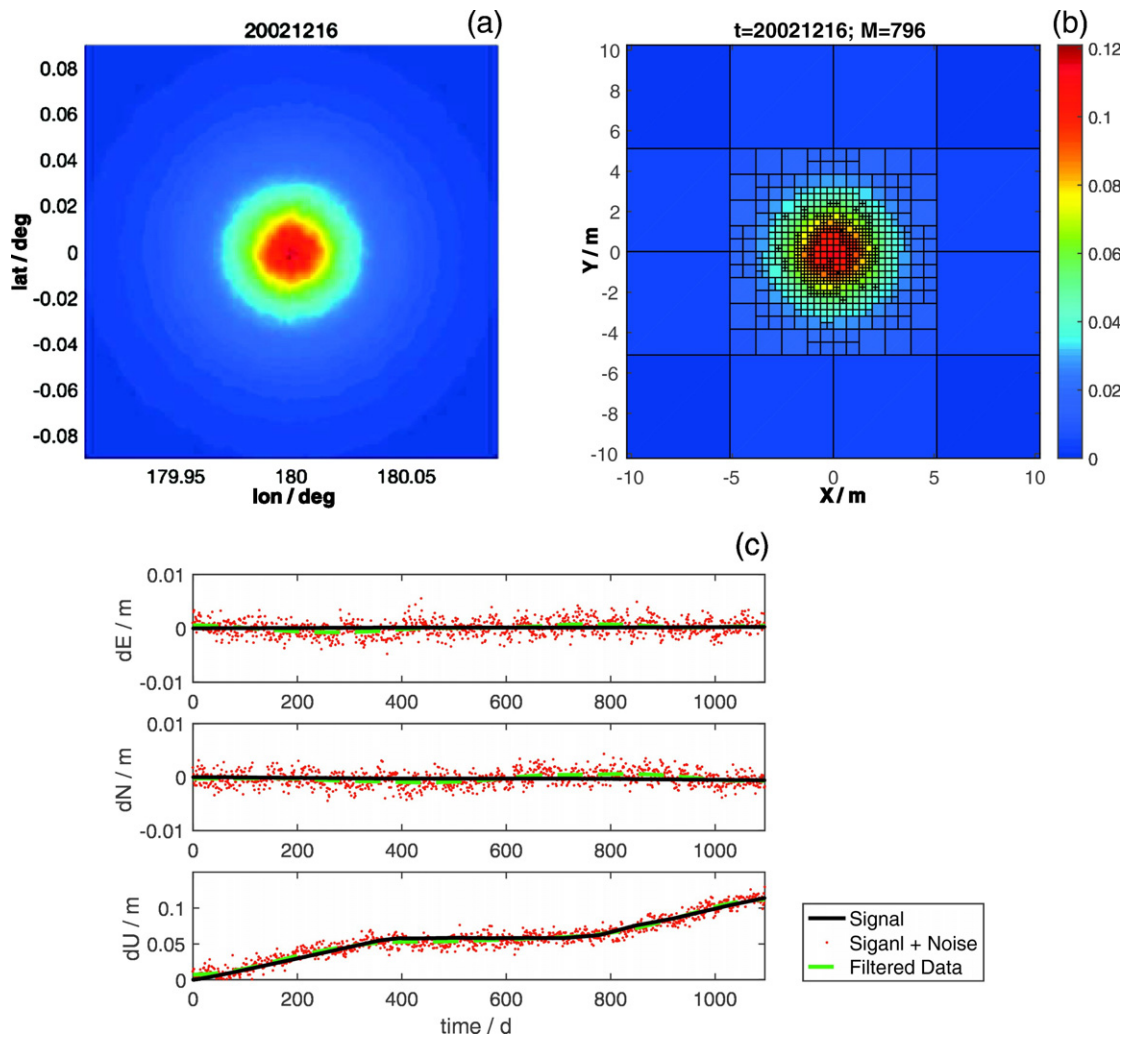


Fig. 4. Synthetic datasets produced by the FEM setup illustrated in Fig. 2. (a) Synthetic InSAR observations of vertical displacement with a distance-correlated noise. (b) Quadtree partition of InSAR data based on root mean square algorithm (Jónsson et al., 2002). (c) Time series of three displacement components for the GPS station at (0, 0). The solid black lines represent the signal of surface deformation from the FEM model. The red dots are the GPS signal which has been perturbed by white and flicker noise. The green dashed lines show the filtered data used in the EnKF analysis.

where \mathbf{I} is an $N_{\text{ens}} \times N_{\text{ens}}$ identity matrix and $\mathbf{1}_{N_{\text{ens}}} \in \mathbb{R}^{N_{\text{ens}} \times N_{\text{ens}}}$ is a matrix where every element equals to $1/N_{\text{ens}}$.

The covariance matrix is calculated by:

$$\mathbf{P}_e = \frac{\mathbf{A}'(\mathbf{A}')^T}{N_{\text{ens}} - 1} \quad (7)$$

The EnKF analysis requires measurements to update the model parameters. In this study, we apply the synthetic observations generated by the FEM described in Section 2.1. The measurements d with their perturbation δd_j are given as:

$$d_j = d + \delta d_j \quad (8)$$

where we assume 10% random perturbation for the measurements. The measurement matrix is then defined as

$$\mathbf{D} = (d_1, d_2, \dots, d_{N_{\text{mes}}}) \in \mathbb{R}^{N_{\text{mes}} \times N_{\text{ens}}} \quad (9)$$

and the ensembles of measurement perturbations, $\delta \mathbf{d}$, is:

$$\delta \mathbf{d} = (\delta d_1, \delta d_2, \dots, \delta d_{N_{\text{ens}}}) \quad (10)$$

from which the covariance matrix for measurements, \mathbf{R}_e , is represented by:

$$\mathbf{R}_e = \frac{\delta \mathbf{d}(\delta \mathbf{d})^T}{N_{\text{ens}} - 1} \quad (11)$$

Finally, the EnKF analysis step combines the models and data to provide a matrix of updated model parameters:

$$\mathbf{A}^a = \mathbf{A} + \mathbf{P}_e \mathbf{H}^T (\mathbf{H} \mathbf{P}_e \mathbf{H}^T + \mathbf{R}_e)^{-1} (\mathbf{D} - \mathbf{H} \mathbf{A}) \quad (12)$$

where \mathbf{H} is the mapping matrix linking the forecast ensemble and the measurements. The EnKF scheme calculates this equation when a new observation becomes available. The size of the parameter space (Γ_p) is computed at the end of each step, to ensure that catastrophic divergence has not occurred (Evensen, 2003, 2009a; Gregg and Pettijohn, 2016).

Two critical updates are developed from the method introduced in Gregg and Pettijohn (2016). First, the EnKF scheme is adapted into 3D by expanding the matrixes to accommodate data and model outputs in the third dimension. Second, additional iterations of the EnKF analysis Eq. (12) are applied before progressing to the next time step. These iterations take advantage of the available observations in the present step and analyze the ensembles from the previous iteration.

2.4. Sensitivity tests and performance evaluation

Ideally, after several EnKF analysis steps, the parameter space and the solution space should shrink significantly and reproduce the parameters assumed in the synthetic model. In reality, the observations are limited both spatially and temporally and may impact the ability of

the EnKF to converge onto a solution. A series of systematic tests are developed to test the performance of the EnKF, which allows us to develop strategies to improve the application of EnKF.

The sensitivity tests (Table 3) include strategies not only for testing the effect of the EnKF setup, such as: (1) the number of ensembles; (2) intra-EnKF iterations between observational time steps; (3) minimum tolerance for the size of the parameter space; and (4) initial parameter values, but also for optimizing data collection and use, including: (5) the location of GPS stations; (6) the number of GPS stations; (7) the temporal continuity of the GPS data stream; and (8) the spatial coverage of InSAR.

The performance of the EnKF analysis is quantified by two values. First, the Root Mean Squared Error (RMSE) provides the fit between the model-predicted surface displacement and the synthetic observations (Gregg and Pettijohn, 2016). Second, the parameter misfit p , a dimensionless value defined as

$$\sigma_p t = \sum_{i=1}^{N_{\text{par}}} \left(\frac{Z_i^t - Z_i^a}{\hat{Z}} \right)^2 \quad (13)$$

where Z_i^t is an assumed parameter used for producing the synthetic data, Z_i^a is the corresponding parameter from the EnKF analysis, and \hat{Z} are the assumed values used to scale the equation to a dimensionless quantity (for horizontal location of the source $\hat{Z} = 10$ km as the half length of the study area). When calculating the misfit, we combine the radius, R , and the overpressure, ΔP , expressing them by the volume change ΔV , since the radius and overpressure are hard to be determined separately in the Mogi (1958) model. In addition, the nature of overpressure is still unclear. According to the Mogi (1958) model, the term $\Delta P a^3$ has a linear relationship with the volume change ΔV , as

$$\Delta V = \frac{\Delta P \cdot V}{K} = \frac{4\pi \Delta P a^3}{3K} \quad (14)$$

where K is the bulk modulus, and the volume change, ΔV , is small compared to the total volume, V .

3. Testing strategies for EnKF implementation

3.1. Variations in the number of ensembles and intra-EnKF iterations

While the EnKF is computationally much less expensive than the traditional Kalman Filter and Extended Kalman Filter techniques, the ensemble-based approach can be very taxing when utilized with large finite element models (e.g., Gregg and Pettijohn, 2016). As such, it is critical to efficiently set up the EnKF in a way that optimizes the computational usage with quantifiable gains in EnKF performance. The largest increase in computation time and storage during EnKF analysis occurs from increasing the number of ensembles. Since each 3D FEM may take on the order of hours to complete and require tens of gigabytes of data storage, adding 100–1000 ensembles may prove computationally prohibitive. Alternatively, intra-EnKF iterations are very swift and require no additional storage because no additional FEM calculations

Table 3
Summary of the sensitivity tests.

Type	Test name	Variable	Values				
EnKF condition	Ensemble number	N_{ens}	50	100	200	500	1000
	Iteration number	$Iterations$	1	2	5	10	50
	Parameter space tolerance	Γ_p (%)	5	10	20	40	80
	Initial parameter (average depth)	d_{avg} (km)	−4.5	−3.5	−3.0	−2.5	−2.0
	Initial parameter (depth range)	d_{inv} (km)	0.5	1.0	2.0	3.0	4.0
	Number of GPS stations	N_{GPS}	20	16	12	8	4
Data collection	Missing GPS station every step	N_{misGPS}	1	2	4	8	16
	Location of GPS-1	$R_{\text{GPS}-1}$ (km)	0.5	1.5	2.5	3.5	4.5
	InSAR spatial coverage	F_{InSAR}	7/8	3/4	1/2	1/4	1/8

are needed to iterate on the EnKF analysis step (Eq. (12)), which can be performed in ~ 10 's of seconds to minutes.

The first suite of synthetic tests investigates the effects of the number of ensembles and number of intra-EnKF iterations to determine which EnKF setup results in the most optimal model convergence and provides a better EnKF prediction most efficiently. Tests of the number of ensembles consist of five EnKF analyses with prescribed N_{ens} ranging from 50 to 1000 (Table 3). Results indicate that, for $N_{ens} \geq 100$, the number of ensembles has little effect on the calculated normalized RMSE of the displacement field (Fig. 5a) when using InSAR data. The parameter misfits of the models with < 100 ensemble members are significantly high, (Fig. 5b), but EnKF runs with > 100 ensembles exhibit obvious advantages. However, the EnKF result does not significantly improve as the ensemble sizes are increased well beyond 100. As discussed below in Section 4.1, these findings are in agreement with previous tests that indicate ensemble numbers as low as 100 may be sufficient for model convergence (Evensen, 2003). An important caveat to this finding is that for natural data, larger ensemble sizes may be necessary to track the dynamic system. When this approach is applied to real data, it will be important to re-test the impact of ensemble number on model convergence. For the GPS data tests, the number of ensembles does not affect the EnKF performance at all when we have > 50 ensembles (Fig. S3a, b). Since the number of measurement at each time step for the GPS data is at least an order less than the ensemble numbers, parameter space with 50 ensembles may already be large enough for the EnKF to obtain a good parameter estimation through a few measurements.

EnKF performance is drastically improved by incorporating an iterative EnKF analysis in between available data time steps when using temporally sparse data sets. As illustrated in Fig. 5c and d, a sudden drop in both the normalized RMSE and parameter misfit is found when additional iterations are applied using InSAR data; However, the improvement of the EnKF's performance appears to plateau when the number of iterations exceeds 10. On the other hand, there does not appear to be a gain in performance when applying an iterative

EnKF analysis to assimilate the GPS data (Fig. S3c, d). The temporally dense nature of the 1000 time-step continuous GPS data stream seems to be more than adequate for the EnKF to converge, and any additional iterations do not offer significant improvements to the analysis.

3.2. Catastrophic filter divergence tolerance

To avoid catastrophic filter divergence, a tolerance parameter, Γ_p , is set to restrict the minimum standard deviation of the parameter distributions determined during the EnKF analysis (Table 3). Both results of the synthetic tests using InSAR and GPS data show that a lower threshold of minimum parameter space make the EnKF perform better (Figs. 5 and S3e, f). The similar pattern also occurs in the RMSEs, where higher tolerance means higher RMSEs and higher standard deviations of the RMSE (Figs. 5e and S3e).

3.3. Initial parameter values

When working with a natural volcanic system, investigators may have a priori information about the location and extent of the magma system. However, typically, initial assessment of unrest from geodetic observations is conducted without any prior knowledge about the source of deformation. Since the EnKF analysis requires an initial guess of the parameter space to create the initial ensemble suite, it is critical to understand the impact of the initial parameter distribution on model performance. As such, we test the impact of different initial parameter suites on the EnKF by varying, first, the average value of depth of the magma reservoir, and, second, the range of the depth (Table 3). Our tests indicate that, for our synthetic InSAR or GPS data, the initial assumptions have little effect on the EnKF RMSEs and the parameter misfits (Figs. 6 and S4). All tests illustrate similar RMSEs ($\sim 2\%$) and parameter misfits, regardless of the initial parameter assumptions. This finding provides reassurance for using the EnKF approach to investigate geodetic observations at systems with little or no prior information.

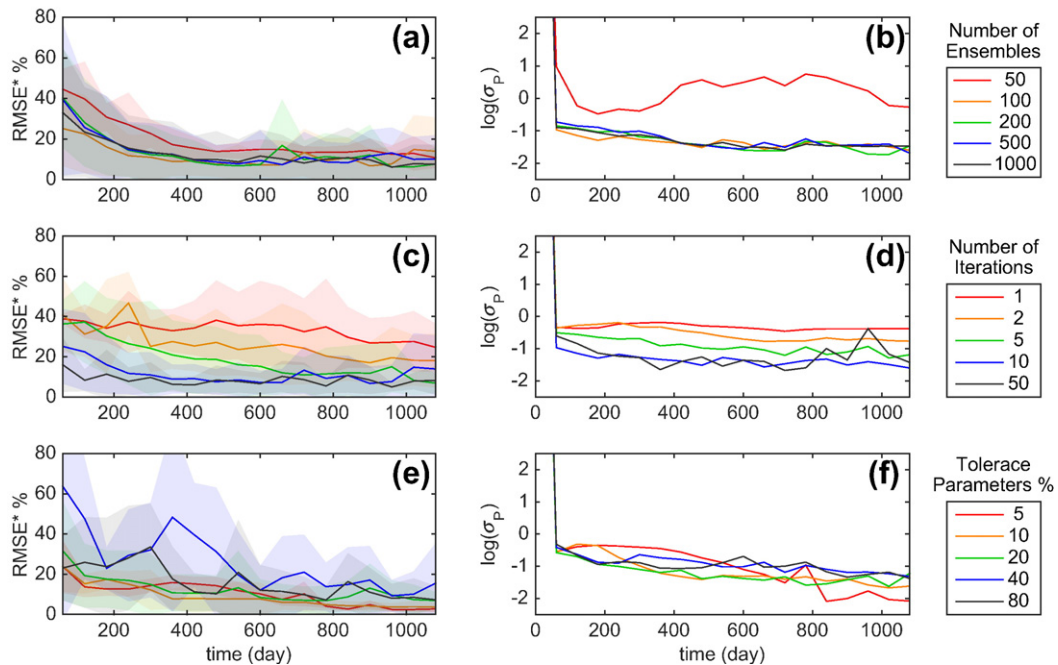


Fig. 5. Sensitivity tests to investigate the effect of the EnKF setup using synthetic InSAR data. (a) and (b) the number of ensembles is varied from 50 to 1000. (a) The calculated normalized RMSE indicates that variations in N_{ens} has very little impact on the ability of the EnKF to match the observed surface displacement. (b) The parameter misfit (in log) illustrates a slightly better fit at higher numbers of ensembles. (c) and (d) the number of intra-EnKF iterations are tested. The calculated normalized RMSE (c) and the parameter misfit (d) both illustrate that the additional of intra-EnKF iterations can significantly improve the model fit. However, this effect is maximized at 10 intra-EnKF iterations. (e) and (f) test variations in the minimum tolerance of the EnKF parameter standard deviation used to compose the EnKF ensembles. While variations in tolerance appear to have a minimal impact in the EnKF's ability to match the surface deformation signal (e), there is a much greater impact on the predicted parameter values. The solid lines in color show the mean values of the normalized root mean square errors (RMSE*) or parameter misfits (σ_p) in log scale. The shadows are the standard deviations.

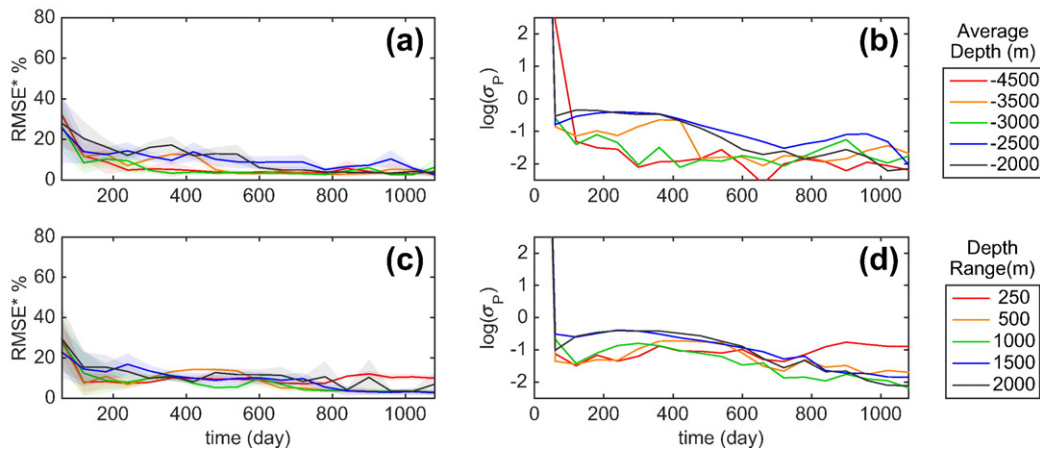


Fig. 6. Sensitivity tests for variations in the initial distribution of magma reservoir depth using synthetic InSAR data. (a) Normalized RMSEs of the displacement field for tests considering different average values of magma reservoir depth, and (c) for tests considering different ranges of magma reservoir depth. (b) Parameter misfits for the “average value” tests, and (d) parameter misfits for “range” tests. The solid lines in color show the mean values of the normalized root mean square errors (RMSE*) or parameter misfits (σ_p) in log scale. The shadows are the standard deviations.

3.4. Geodetic data coverage and quality

In the previous sections, we tested the setup and workflow of the EnKF approach and found that the greatest enhancement to EnKF performance comes from conducting intra-EnKF iterations between observation time steps to improve the filter convergence on temporally sparse data sets. We also illustrated that EnKF performance is relatively insensitive to the number of ensembles and the initial parameter distributions. The previous experiments were all conducted using optimal data coverage, and as can be expected, the quality of the observational inputs directly affects the performance of the EnKF analysis. The goal of the next series of synthetic tests is to determine which observations provide better constraints for the EnKF analysis. We conduct four tests to consider both the spatial and temporal distribution of GPS and InSAR observations and devise strategies for future data collection and assimilation efforts. In the following tests, the parameter misfits are utilized to indicate the quality of the results, since the RMSEs are heavily biased by the variations in data distribution.

3.4.1. InSAR coverage

InSAR is a powerful tool for observing the onset of unrest at previously dormant volcanoes (Massonnet and Feigl, 1998; Lu et al., 2000; Chaussard et al., 2013; Pinel et al., 2014; Masterlark et al., 2016b). The source estimation using InSAR data can provide important context for future data collection efforts including a signal to optimize data collection strategies. However, the lack of InSAR data coverage may adversely impact its assimilation and the performance of the EnKF. In the InSAR coverage test, we consider two potential gaps in InSAR data (1) a topographic shadow zone restricting observations in a region of a volcano due to a volcanic edifice, and (2) a circular shadow in the center of volcano deformation created by snow or ice cover.

In the topographic shadow test, the InSAR measurements are masked over a fraction of the volcano, ranging from 12.5% to 87.5% (Fig. S2). The results indicate that the parameter misfits with more extensive InSAR data coverage are lower than models utilizing masked InSAR coverage (Fig. 7d). This is particularly noticeable in predictions of the horizontal location of the magma reservoir, which is not well constrained in models with extensive InSAR LOS shadows (Fig. S8). This effect illustrates that the percentage of InSAR data coverage affects the quality of the EnKF analysis. Our numerical tests indicate that as coverage decreases <50% EnKF performance is adversely impacted and parameter values are not as well constrained. Similarly, restricting data coverage at the center of the volcano due to snow cover will not

significantly impact EnKF performance (Fig. S8). However less snow coverage enhance the ability of the EnKF to tracking the correct reservoir depth, which is similar to the results observed in the GPS distance tests in the next section.

Overall, InSAR data are quite robust, providing excellent observational inputs for the EnKF, even with sparse temporal observations (e.g., Gregg and Pettijohn, 2016) and spatial limitations. In the next section, limitations posed by GPS data are investigated to determine how best to optimize on-the-ground deformation observations.

3.4.2. GPS station availability

While InSAR data tend to be spatially rich, providing extensive coverage for a region surrounding a volcano, GPS data may provide rich temporal information in discrete locations. The initial “optimal” locations of the 20 GPS stations used in the previous sensitivity tests are shown in Fig. S1. However, typically, volcanoes may only be instrumented by a few stations and often times may only have data available from yearly campaigns. In our first synthetic test, we look specifically at the limitations posed by station availability and seek to address the situation where only a few instruments are available for data collection. In the model tests, at each time step four GPS stations are removed randomly, until only the four GPS stations remain. The test shows that the misfits gradually increase with the decreasing number of GPS stations, and the calculated parameters significantly deviate from the synthetic values when more than half of the GPS stations are removed (Figs. 7b and S5). As illustrated in Fig. 7b, as the number of continuous stations is reduced to 4 or less, there is significant increase in the parameter misfit. In a real world data collection effort, one may take this result to indicate that having only four continuous stations may be prohibitive for efficient use of the EnKF. However, as we will show in the following section, strategies such as episodically moving instruments to occupy a larger range of locations can significantly enhance GPS data collection when station availability is limited.

3.4.3. GPS data continuity

In the previous section, we illustrated the impact of data scarcity on the ability of the EnKF to accurately predict parameter values. Another potential limitation of GPS is the loss of station functionality during deployment, which may result in prolonged gaps in the GPS data stream. To mimic this situation, we conduct a test in which random GPS stations (from 1 station and 16 stations concurrently) switch off (Fig. S6 and Table 3) to create “gaps” in our synthetic data (Fig. S1). The misfit plot shows that data discontinuities do not significantly impact the EnKF’s ability find the assumed parameters (Fig. 7c). Although leaving only

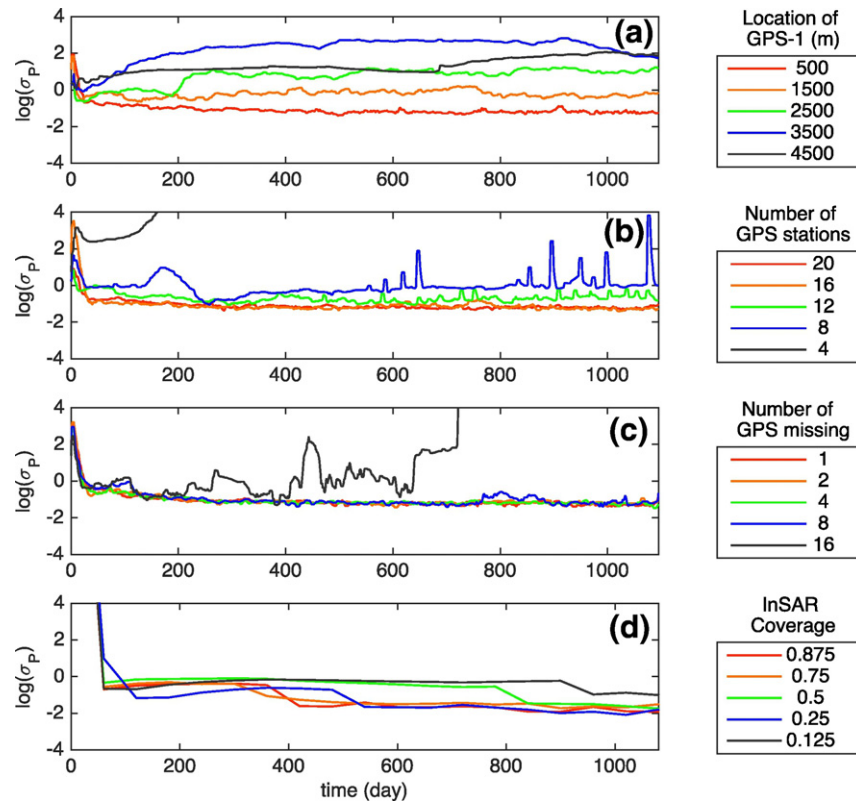


Fig. 7. Parameter misfits for sensitivity tests investigating strategies for utilizing spotty GPS and InSAR data. (a) Variations in the distance between the nearest GPS station, GPS-1 (Fig. 4a), and the center of uplift. (b) Variation in the total number of available GPS stations. (c) Variations in the number of GPS stations, which do not work at each time step (Fig. S1). (d) Fraction of the region surrounding the center of volcanic uplift where InSAR data are not available (see Supplemental Fig. S2). The solid lines in color show the mean value of the parameter misfits (σ_P) in log scale (σ_P) in log scale.

four GPS stations working at a given time makes EnKF lost, the performance using eight active GPS stations each time step, but moving them effectively is as good as using all station. Effectively, if only a limited number of GPS instruments are available, they will provide a similar EnKF performance as having a larger number of operational instruments as long as the stations are episodically moved to occupy more sites around the region of unrest. Of course, moving permanent stations is unrealistic, so supplementing a low number of permanent stations with campaign station observations from a variety of locations may be an effective strategy for improving model performance.

3.4.4. GPS station locations

The previous section focused on the number of GPS station locations necessary to provide a robust data stream for the EnKF. It is also important to optimize the locations of the installed GPS stations. In particular, when establishing permanent, continuous stations near a restless volcano, potential risks may prohibit installation at the center of deformation. In this section, a series of tests are conducted to illustrate the impact of installing GPS stations further away from the loci of unrest. In other words, the distance between the first GPS station (GPS-1 in the Fig. S1) and the center of deformation is varied from 0.5 km to 4.5 km (Table 3). The results show that the EnKF performs much better when the GPS stations are closer to the volcano (Fig. S7 and Fig. 7a), and indicate that having a deformation signal at the center of uplift can greatly improve model fit.

4. Discussion

4.1. Optimizing the EnKF setup

One of the advantages of using the Ensemble Kalman Filter (EnKF) is computational economy, which is greatly improved over other data

assimilation methods, such as the traditional Kalman Filter or the Extended Kalman Filter (Evensen, 2009a; Gregg and Pettijohn, 2016). However, when a larger ensemble space is introduced, the computational cost is greatly increased since each ensemble requires an independent model solution. In this study, we use the analytical solution from Mogi (1958) to calculate the forecast ensembles, which is computationally swift. However, a finite element approach as used by Gregg and Pettijohn (2016) will take upwards of 20 h for an EnKF analysis with 100 ensembles run for 100 days, in 2D and several days to run in 3D.

Our synthetic tests using either InSAR or GPS data indicate that the EnKF performance is considerably enhanced when using 100 ensemble over using only 50 ensembles. This suggests, at least in this simple volcano reservoir modeling with less than ten unknown parameters, a minimum value of 50 ensemble members (Evensen, 2009a) is sufficient. Utilizing fewer FEMs in the ensemble greatly reduces the computational cost, especially as more sophisticated reservoir models are applied (Simakin and Ghassemi, 2010; Gregg et al., 2012; Ronchin et al., 2013; de Silva and Gregg, 2014; Cannavò et al., 2015). However, when applying the EnKF to natural data sets in future investigations, it will be important to establish a critical minimum value for the number of ensembles, which may vary from system to system depending on the unrest dynamics.

Compared to increasing the number of ensembles, utilizing additional iterations between data assimilation time steps when applying InSAR data is a far more economical way to improve the EnKF performance. Usually, an InSAR image contains about 1000 measurement points even after down-sampling. Therefore, the EnKF requires more iterations to converge on a solution. However, the GPS measurements are far less than InSAR, and one iteration may be enough. The iteration test in Section 3.1 indicates that the RMSEs and parameter misfits are greatly reduced, even if only one additional iteration is introduced

(Fig. 5c and d). The cost of applying more iterations can be estimated by the Eq. (12), which is $\sim N_{dim} \times N_{ens}^2$ (Evensen, 2003). Assuming we apply 100 ensembles and have 1000 measurements at every step, the computational costs of calculating A is around the order of 10^7 . If we use a linear elastic finite element model, which takes the topography into account, to calculate the forecasting ensemble and we assume the finite element mesh creates 10^5 nodes and corresponding degrees of freedom, which is 10 times more than the synthetic model in this study. The computational cost is $>10^{10}$ for every ensemble per step, which is three orders of magnitude greater than applying one additional iteration. In summary, applying several more iterations between time steps is a much more efficient way to improve the EnKF analysis and is doable with far less computational cost.

4.2. Does a better initial guess lead to a better solution?

As opposed to other data assimilation methods such as genetic algorithms (Barth, 1992), the EnKF requires a presumption of the initial parameter distributions to produce the initial ensembles created by a Monte Carlo method (Evensen, 2009a). Parameters such as location and geometry of a magma reservoir are not well constrained unless additional geophysical observations or a priori information are available. However, the precise structure beneath many restless volcanoes, for example the volcanoes in the Sunda Arc of Indonesia, are still unknown (Chaussard and Amelung, 2014). The lack of certainty for the source parameters of the observed surface deformation might be problematic for creating an initial guess of the parameters for the magma reservoir. Furthermore, some parameters such as volume changes and pressure changes in the magma reservoir cannot be directly measured.

Fortunately, synthetic tests of varying the initial parameter guesses indicate that the distribution of the initial parameters has little to no

effect on the value of the updated parameters after several steps of EnKF analysis (Figs. 6 and S4). Therefore, although the initial guess for the modeling parameters is needed in the EnKF analysis, a better guess of the model parameters does not necessarily lead to a better EnKF performance, meaning that the stability of this scheme is parametrically unconditional.

4.3. Improving data assimilation with better data

How the measurements affect the predictive performance of data assimilation schemes is of great concern to geodesists, since model predictions must be optimized with spatially and temporally limited data sets. This is especially pertinent for the collection of continuous GPS data, which requires that GPS station locations to be chosen, instrumented, and maintained; this costs time, money, and the inherent risk of installing a GPS station close to an active volcano. From the GPS location synthetic test, we conclude that the closer a GPS station is to the loci of deformation, the better the EnKF performance (Fig. 7a). However, to determine how close a GPS station needs to be installed, multiple EnKF experiments can be run on existing data to determine the critical distance for establishing a GPS station.

Just as instrument location is critical for constraining the evolution of a magma chamber, the number of available instruments is also key. Given the financial considerations of installing and maintaining GPS stations, optimizing station location with number of instruments can be critical for providing optimal data coverage. As one might expect, our synthetic tests indicate that having fewer GPS stations results in larger misfits in the EnKF analysis (Fig. 7b). Credible results are not achieved with <8 GPS stations (Fig. 7b), unless the stations are occasionally relocated to different places, which is indicated by the GPS temporal continuity test (Fig. 7c). In Fig. 7c, we find that even if only 8 GPS

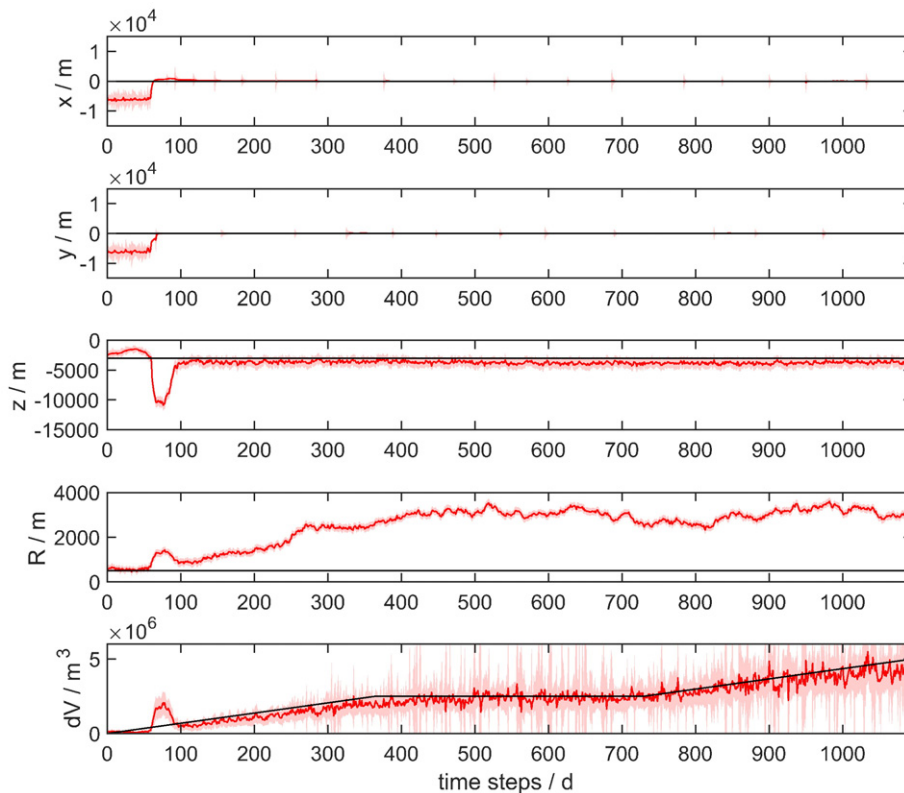


Fig. 8. The parameter estimation of a joint InSAR and GPS data assimilation. The EnKF analysis uses 100 ensembles with 10 iterations. The minimum tolerance for parameter space is 20%. The synthetic GPS station locations are shown at Fig. 4, where the distance of GPS-1 is 0.5 km. The red solid lines with shadows show the estimation of the parameters by EnKF analysis, and the black solid lines represent the parameters assumed in the synthetic model. It costs only about 100 days for the EnKF to capture the assumed values. Although, the EnKF is unable to find the real radius due to non-uniqueness, the EnKF is able to find the evolution of the volume changes within the magma reservoir.

stations are working at a given time, the EnKF analysis can provide as accurate of a result as a model with 20 continuous GPS stations. Therefore, if only a limited number of campaign GPS instruments are available, shifting them between several locations to provide discontinuous data for multiple locations is a better way to provide constraints for data assimilation, than to keep them steady in one location to provide continuous data.

InSAR measurements are routinely affected by the snow, ice, and atmospheric interference, and/or topography which can limit the coverage over a study area (Massonnet and Feigl, 1998). Especially in a volcano study, a topographically high volcano edifice may result in an InSAR LOS shadow and limit InSAR data coverage on one side of a volcano (Chaussard and Amelung, 2012; Chaussard et al., 2013). Our synthetic tests of InSAR data coverage (Fig. S2 and Fig. 7d), indicate that EnKF performance is seldom affected by the coverage of the InSAR data. However, in this axisymmetric, synthetic study the percentage of the study area not covered by InSAR measurement is offset by information provided by InSAR coverage from other sections of the volcano, similar to what was observed in the 2D EnKF applications (Gregg and Pettijohn, 2016). On the other hand, if the data are missing from a significant region of the volcano, due to snow or atmospheric artifacts, the EnKF derived parameters will not be well constrained (Figs. 7d, S8 and S9).

Compared to the InSAR data (Fig. S8) GPS data create better predictions on the evolution of the magma volume change (Figs. S5 to S7). However, the EnKF can find the assumed parameters in fewer steps using InSAR data than using GPS data when applying iterative analysis. The joint assimilation of GPS and InSAR data provides the best estimation of the parameters of the magma reservoir (Gregg and Pettijohn, 2016) especially when the abundant data are supplied (Fig. 8). Furthermore, applying data assimilation with present data also provides information for future data collection. For example, establishing GPS stations in the area where InSAR data is not available will help to constrain estimations of a magma reservoir's location (Fig. 8).

Ultimately, one of the advantages to the EnKF approach is that it allows investigators to test data collection schemes and optimize future efforts at active volcanoes. InSAR can be used to set the stage for on-the-ground observations, which will in turn enhance future InSAR data collection efforts. While this particular investigation focuses on ground deformation and geodesy, the results provided by InSAR and GPS data assimilation will also inform additional geophysical data collection efforts such as gravity, tomography, and magnetotellurics.

4.4. The issue of non-uniqueness

The EnKF analysis sometimes results in poor performance due to the issue of non-uniqueness when a complicated system is being described by an over simplified model (Evensen, 2009a; Baehr et al., 2010; Jafarpour and Tarrahi, 2011). For the case of a deforming volcano, magma reservoir evolution is a highly non-unique problem and the same surface displacement may be generated by multiple combinations of reservoir location, geometry, and overpressure according to Eqs. (3) and (4) (Gregg and Pettijohn, 2016). This issue is particularly pronounced when using the elegant, but simple Mogi elastic model. Enlarging the size of the parameter space is a way to produce more parametric combinations and give the EnKF more options for optimization (Fig. 5e and f); however, this will not solve the problem of distinguishing which combination is the true solution.

An alternative approach is to combine two or more parameters in the Mogi (1958) model into one, as we did in this study, replacing reservoir radius and overpressure with volume change. During the tests, the predicted volume change, ΔV , is more consistent with the exact value in the synthetic model, while the radius or overpressure are not as close to the assumed value as the volume change (Fig. 8), since there are numerous non-unique combination of overpressure and radius that satisfy a certain volume change.

In future efforts, more types of measurements and more sophisticated models should be introduced to provide additional constraints on the overpressure or geometrical properties of the source of unrest. Additional geophysical observations such as tomography (Burnett et al., 1989; Day et al., 2001; Lees, 2007; Stankiewicz et al., 2010) may provide important constraints on magma chamber radius. In other words, assimilating geophysical observations that constrain the geometry of the magmatic system will allow future EnKF investigations to infer the magma storage evolution.

5. Conclusions

Developing data assimilation strategies to incorporate the vast array of volcano monitoring data sets into increasingly more sophisticated geodynamics models is critical for future efforts to assess volcanic unrest. Fields such as climate science, hydrology, and physical oceanography have long used statistical data assimilation approaches to provide forecasts and model updates from large disparate datasets (e.g. Julier et al., 2000; Bertino et al., 2003; Julier et al., 2004; Evensen, 2003, 2009a, 2009b; Dumedah et al., 2011; Dumedah, 2012). In an effort to build a data assimilation framework for volcano applications, we have developed the widely used Ensemble Kalman Filter (EnKF) sequential data assimilation method in 3D and conducted a series of sensitivity tests using synthetic observations of surface deformation. The sensitivity tests give us insights into how to improve the EnKF performance for volcano applications and optimize both the data assimilation strategy and future data collection efforts.

The results of our sensitivity tests reveal that one may greatly improve the data assimilation efficiency with little computational expense by utilizing additional EnKF analysis iterations between observations time steps. Alternatively, we find that increasing the number of ensemble members to >100, the computational costs of which is at least 1000 times more than using an intra-EnKF iteration strategy, does not provide a significant gain in model convergence. Another great advantage of the EnKF method is that the stability of the EnKF method does not depend on the initial parameter guess. Specifically, tests of the impact of the initial parameter guess indicate that the parameter assumption is unconditional and that the accuracy of the initial guess has no impact on the EnKF performance.

Tests of data collection strategies provide guidance for future data collection efforts. In particular, tests for where the most proximal GPS station must be placed to provide sufficient data coverage encourage geodesists to establish the GPS station closer to the volcano uplift center. Furthermore, if the availability of GPS equipment is limited, shifting instruments between several locations to record discontinuous data provides a better data stream for data assimilation than installing a small number of stations at fixed locations. Finally, InSAR data gaps due to atmospheric noise, snow cover, or topography shadows may not significantly impact its effectiveness, unless major portions of the volcano are masked.

Acknowledgements

We would like to acknowledge helpful discussions with F. Amelung, Y. Aoki, E. Chaussard, and J. Pettijohn. We would also like to thank Dr. Michael Poland and two anonymous reviewers for their comments which greatly improved our manuscript. Development of data assimilation methods for monitoring active volcanoes using InSAR is funded by NASA (13-ES113-0034).

Appendix A. Supplementary data

Supplementary data to this article can be found online at <http://dx.doi.org/10.1016/j.jvolgeores.2017.02.015>.

References

- Agram, P.S., Simons, M., 2015. A noise model for InSAR time series: Agram and Simons. *J. Geophys. Res. Solid Earth* 120:2752–2771. <http://dx.doi.org/10.1002/2014JB011271>.
- Allen, J.I., Eknes, M., Evensen, G., 2003. An ensemble Kalman filter with a complex marine ecosystem model: hindcasting phytoplankton in the Cretan Sea. *Ann. Geophys.* 21: 399–411. <http://dx.doi.org/10.5194/angeo-21-399-2003>.
- Alparone, S., Bonaccorso, A., Bonforte, A., Currenti, G., 2013. Long-term stress-strain analysis of volcano flank instability: the eastern sector of Etna from 1980 to 2012: long-term strain of Etna unstable flank. *J. Geophys. Res. Solid Earth* 118:5098–5108. <http://dx.doi.org/10.1002/jgrb.50364>.
- Anderson, K., Segall, P., 2013. Bayesian inversion of data from effusive volcanic eruptions using physics-based models: application to Mount St. Helens 2004–2008. *J. Geophys. Res. Solid Earth* 118:2017–2037. <http://dx.doi.org/10.1002/jgrb.50169>.
- Baehr, C., Pannekoucke, O., et al., 2010. Some issues and results on the EnKF and particle filters for meteorological models. *Chaotic Syst. Theory Appl.* (27–24).
- Barth, N.H., 1992. Oceanographic experiment design II: genetic algorithms. *J. Atmos. Ocean. Technol.* 9, 434–443.
- Battaglia, M., Segall, P., Murray, J., Cervelli, P., Langbein, J., 2003a. The mechanics of unrest at Long Valley caldera, California: 1. Modeling the geometry of the source using GPS, leveling and two-color EDM data. *J. Volcanol. Geotherm. Res.* 127:195–217. [http://dx.doi.org/10.1016/S0377-0273\(03\)00170-7](http://dx.doi.org/10.1016/S0377-0273(03)00170-7).
- Battaglia, M., Segall, P., Roberts, C., 2003b. The mechanics of unrest at Long Valley caldera, California. 2. Constraining the nature of the source using geodetic and micro-gravity data. *J. Volcanol. Geotherm. Res.* 127:219–245. [http://dx.doi.org/10.1016/S0377-0273\(03\)00171-9](http://dx.doi.org/10.1016/S0377-0273(03)00171-9).
- Beauducel, F., Cornet, F.H., 1999. Collection and three-dimensional modeling of GPS and tilt data at Merapi volcano, Java. *J. Geophys. Res.* 104, 725–736.
- Bertino, L., Evensen, G., Wackernagel, H., 2003. Sequential data assimilation techniques in oceanography. *Int. Stat. Rev.* 71, 223–241.
- Bevis, M., Foster, J., 2000. January 30, 1997 eruptive event in Kilauea Volcano, Hawaii as monitored by continuous GPS. *Geophys. Res. Lett.* 27, 2757–2760.
- Biggs, J., Ebmeier, S.K., Aspinall, W.P., Lu, Z., Pritchard, M.E., Sparks, R.S.J., Mather, T.A., 2014. Global link between deformation and volcanic eruption quantified by satellite imagery. *Nat. Commun.* 5.
- Bonforte, A., Puglisi, G., 2003. Magma uprising and flank dynamics on Mount Etna volcano, studied using GPS data (1994–1995). *J. Geophys. Res. Solid Earth* 108.
- Bonforte, A., Puglisi, G., 2006. Dynamics of the eastern flank of Mt. Etna volcano (Italy) investigated by a dense GPS network. *J. Volcanol. Geotherm. Res.* 153, 357–369.
- Brusdal, K., Brankart, J.M., Halberstadt, G., Evensen, G., Brasseur, P., van Leeuwen, P.J., Dombrowsky, E., Verron, J., 2003. A demonstration of ensemble-based assimilation methods with a layered OGCM from the perspective of operational ocean forecasting systems. *J. Mar. Syst.* 40:253–289. [http://dx.doi.org/10.1016/S0924-7963\(03\)00021-6](http://dx.doi.org/10.1016/S0924-7963(03)00021-6).
- Burnett, M.S., Caress, D.W., Orcutt, J.A., 1989. Tomographic Image of the Magma Chamber at 12° 50' N on the East Pacific Rise.
- Cannavò, F., Camacho, A.G., González, P.J., Mattia, M., Puglisi, G., Fernández, J., 2015. Real time tracking of magmatic intrusions by means of ground deformation modeling during volcanic crises. *Sci. Rep.* 5.
- Carbone, D., Currenti, G., Del Negro, C., 2007. Elastic model for the gravity and elevation changes before the 2001 eruption of Etna volcano. *Bull. Volcanol.* 69:553–562. <http://dx.doi.org/10.1007/s00445-006-0090-5>.
- Chaussard, E., Amelung, F., 2012. Precursory inflation of shallow magma reservoirs at west Sunda volcanoes detected by InSAR: InSAR Survey of west Sunda volcanoes. *Geophys. Res. Lett.* 39. <http://dx.doi.org/10.1029/2012GL053817> (n/a–n/a).
- Chaussard, E., Amelung, F., 2014. Regional controls on magma ascent and storage in volcanic arcs. *Geochim. Geophys. Geosyst.* 15:1407–1418. <http://dx.doi.org/10.1002/2013GC005216>.
- Chaussard, E., Amelung, F., Aoki, Y., 2013. Characterization of open and closed volcanic systems in Indonesia and Mexico using InSAR time series: InSAR time series in Indonesia and Mexico. *J. Geophys. Res. Solid Earth* 118:3957–3969. <http://dx.doi.org/10.1002/jgrb.50288>.
- Cianetti, S., Giunchi, C., Casarotti, E., 2012. Volcanic deformation and flank instability due to magmatic sources and frictional rheology: the case of Mount Etna. *Geophys. J. Int.* 191, 939–953.
- Currenti, G., Del Negro, C., Ganci, G., 2007. Modelling of ground deformation and gravity fields using finite element method: an application to Etna volcano. *Geophys. J. Int.* 169:775–786. <http://dx.doi.org/10.1111/j.1365-246X.2007.03380.x>.
- Day, A.J., Peirce, C., Sinha, M.C., 2001. Three-dimensional crustal structure and magma chamber geometry at the intermediate-spreading, back-arc Valu Fa Ridge, Lau Basin—results of a wide-angle seismic tomographic inversion. *Geophys. J. Int.* 146, 31–52.
- Del Negro, C., Currenti, G., Scandura, D., 2009. Temperature-dependent viscoelastic modeling of ground deformation: application to Etna volcano during the 1993–1997 inflation period. *Phys. Earth Planet. Inter.* 172, 299–309.
- Desmarais, E.K., Segall, P., 2007. Transient deformation following the 30 January 1997 dike intrusion at Kilauea volcano, Hawai'i. *Bull. Volcanol.* 69:353–363. <http://dx.doi.org/10.1007/s00445-006-0080-7>.
- Dmitrieva, K., Segall, P., DeMets, C., 2015. Network-based estimation of time-dependent noise in GPS position time series. *J. Geod.* 89:591–606. <http://dx.doi.org/10.1007/s00190-015-0801-9>.
- Dumedah, G., 2012. Formulation of the evolutionary-based data assimilation, and its implementation in hydrological forecasting. *Water Resour. Manag.* 26:3853–3870. <http://dx.doi.org/10.1007/s11269-012-0107-0>.
- Dumedah, G., Berg, A.A., Wineberg, M., 2011. An integrated framework for a joint assimilation of brightness temperature and soil moisture using the nondominated sorting genetic algorithm II. *J. Hydrometeorol.* 12:1596–1609. <http://dx.doi.org/10.1175/JHM-D-10-05029.1>.
- Emardson, T.R., Simons, M., Webb, F.H., 2003. Neutral atmospheric delay in interferometric synthetic aperture radar applications: statistical description and mitigation. *J. Geophys. Res. Solid Earth* 108:2231. <http://dx.doi.org/10.1029/2002JB001781>.
- Evensen, G., 2003. The ensemble Kalman filter: theoretical formulation and practical implementation. *Ocean Dyn.* 53:343–367. <http://dx.doi.org/10.1007/s10236-003-0036-9>.
- Evensen, G., 2009a. *Data Assimilation*. Springer, Berlin Heidelberg, Berlin, Heidelberg.
- Evensen, G., 2009b. The ensemble Kalman filter for combined state and parameter estimation. *IEEE Control. Syst. Mag.* 29:83–104. <http://dx.doi.org/10.1109/MCS.2009.932223>.
- Fattahi, H., Amelung, F., 2015. InSAR bias and uncertainty due to the systematic and stochastic tropospheric delay: InSAR uncertainty tropospheric delay. *J. Geophys. Res. Solid Earth* 120:8758–8773. <http://dx.doi.org/10.1002/2015JB012419>.
- Gregg, P.M., de Silva, S.L., Grosfils, E.B., 2013. Thermomechanics of shallow magma chamber pressurization: implications for the assessment of ground deformation data at active volcanoes. *Earth Planet. Sci. Lett.* 384:100–108. <http://dx.doi.org/10.1016/j.epsl.2013.09.040>.
- Gregg, P.M., de Silva, S.L., Grosfils, E.B., Parmigiani, J.P., 2012. Catastrophic caldera-forming eruptions: thermomechanics and implications for eruption triggering and maximum caldera dimensions on earth. *J. Volcanol. Geotherm. Res.* 241:242:1–12. <http://dx.doi.org/10.1016/j.jvolgeores.2012.06.009>.
- Gregg, P.M., Pettijohn, C., 2015. *A Multi-data Stream Assimilation Framework for the Assessment of Volcanic Unrest*.
- Gregg, P.M., Pettijohn, J.C., 2016. A multi-data stream assimilation framework for the assessment of volcanic unrest. *J. Volcanol. Geotherm. Res.* 309:63–77. <http://dx.doi.org/10.1016/j.jvolgeores.2015.11.008>.
- Grosfils, E.B., 2007. Magma reservoir failure on the terrestrial planets: assessing the importance of gravitational loading in simple elastic models. *J. Volcanol. Geotherm. Res.* 166:47–75. <http://dx.doi.org/10.1016/j.jvolgeores.2007.06.007>.
- Grosfils, E.B., McGovern, P.J., Gregg, P.M., Galgana, G.A., Hurwitz, D.M., Long, S.M., Chestler, S.R., 2015. Elastic models of magma reservoir mechanics: a key tool for investigating planetary volcanism. In: Platz, T., Massironi, M., Byrne, P.K., Hiesinger, H. (Eds.), *Volcanism and Tectonism Across the Inner Solar System*. Geological Soc Publishing House, Bath, pp. 239–267.
- Hickey, J., Gottsmann, J., del Potro, R., 2013. The large-scale surface uplift in the Altiplano-Puna region of Bolivia: a parametric study of source characteristics and crustal rheology using finite element analysis. *Geochim. Geophys. Geosyst.* 14:540–555. <http://dx.doi.org/10.1002/ggge.20057>.
- Hickey, J., Gottsmann, J., Mothes, P., 2015. Estimating volcanic deformation source parameters with a finite element inversion: the 2001–2002 unrest at Cotopaxi volcano, Ecuador. *J. Geophys. Res. Solid Earth* 120:1473–1486. <http://dx.doi.org/10.1002/2014JB011731>.
- Jafarpour, B., Tarrahi, M., 2011. Assessing the performance of the ensemble Kalman filter for subsurface flow data integration under variogram uncertainty. *Water Resour. Res.* 47. <http://dx.doi.org/10.1029/2010WR009090>.
- Jónsson, S., Zebker, H., Segall, P., Amelung, F., 2002. Fault slip distribution of the 1999 Mw 7.1 Hector Mine, California, earthquake, estimated from satellite radar and GPS measurements. *Bull. Seismol. Soc. Am.* 92, 1377–1389.
- Julier, S.J., Julier, S.J., Uhlmann, J.K., 2004. Unscented filtering and nonlinear estimation. *Proc. IEEE* 92:401–422. <http://dx.doi.org/10.1109/jproc.2003.823141>.
- Julier, S., Uhlmann, J., Durrant-Whyte, H.F., 2000. A new method for the nonlinear transformation of means and covariances in filters and estimators. *IEEE Trans. Autom. Control* 45:477–482. <http://dx.doi.org/10.1109/9.847726>.
- Kalman, R.E., 1960. A new approach to linear filtering and prediction problems. *J. Fluids Eng.* 82, 35–45.
- Le Mével, H., Feigl, K.L., Córdova, L., DeMets, C., Lundgren, P., 2015. Evolution of unrest at Laguna del Maule volcanic field (Chile) from InSAR and GPS measurements, 2003 to 2014. *Geophys. Res. Lett.* 42, 6590–6598.
- Lees, J.M., 2007. Seismic tomography of magmatic systems. *J. Volcanol. Geotherm. Res.* 167:37–56. <http://dx.doi.org/10.1016/j.jvolgeores.2007.06.008>.
- vanLeeuwen, P.J., Evensen, G., 1996. Data assimilation and inverse methods in terms of a probabilistic formulation. *Mon. Weather Rev.* 124:2898–2913. [http://dx.doi.org/10.1175/1520-0493\(1996\)124<2898:DAAIMI>2.0.CO;2](http://dx.doi.org/10.1175/1520-0493(1996)124<2898:DAAIMI>2.0.CO;2).
- Lisaeter, K.A., Evensen, G., Laxon, S., 2007. Assimilating synthetic CryoSat sea ice thickness in a coupled ice-ocean model. *J. Geophys. Res. Oceans Atmos.* 112, C07023. <http://dx.doi.org/10.1029/2006JC003786>.
- Lohman, R.B., Simons, M., 2005. Some thoughts on the use of InSAR data to constrain models of surface deformation: noise structure and data downsampling: thoughts on InSAR. *Geochim. Geophys. Geosyst.* 6. <http://dx.doi.org/10.1029/2004GC000841> (n/a–n/a).
- Lu, Z., Dzurisin, D., Biggs, J., Wicks, C., McNutt, S., 2010. Ground surface deformation patterns, magma supply, and magma storage at Okmok volcano, Alaska, from InSAR analysis: 1. Intereruption deformation, 1997–2008. *J. Geophys. Res. Solid Earth* 115: B00B02. <http://dx.doi.org/10.1029/2009JB006969>.
- Lu, Z., Mann, D., Freymueller, J.T., Meyer, D.J., 2000. Synthetic aperture radar interferometry of Okmok volcano, Alaska: radar observations. *J. Geophys. Res. Solid Earth* 105, 10791–10806.
- Mao, A., Harrison, C.G.A., Dixon, T.H., 1999. Noise in GPS coordinate time series. *J. Geophys. Res. Solid Earth* 104:2797–2816. <http://dx.doi.org/10.1029/1998JB900033>.
- Massonnet, D., Feigl, K.L., 1998. Radar interferometry and its application to changes in the Earth's surface. *Rev. Geophys.* 36, 441–500.

- Masterlark, T., Donovan, T., Feigl, K.L., Haney, M., Thurber, C.H., Tung, S., 2016a. Volcano deformation source parameters estimated from InSAR: sensitivities to uncertainties in seismic tomography: volcano deformation source parameters. *J. Geophys. Res. Solid Earth* 121:3002–3016. <http://dx.doi.org/10.1002/2015JB012656>.
- Masterlark, T., Donovan, T., Feigl, K.L., Haney, M., Thurber, C.H., Tung, S., 2016b. Volcano deformation source parameters estimated from InSAR: sensitivities to uncertainties in seismic tomography. *J. Geophys. Res. Solid Earth* 121, 3002–3016.
- McTigue, D.F., 1987. Elastic stress and deformation near a finite spherical magma body: resolution of the point source paradox. *J. Geophys. Res.* 92:12931. <http://dx.doi.org/10.1029/jb092ib12p12931>.
- Mogi, K., 1958. Relations between the eruptions of various volcanoes and the deformations of the ground surfaces around them. *Bull. Earthq. Res. Inst., University of Tokyo* 36, 99–134.
- Morales Rivera, A.M., Amelung, F., Eco, R., 2015. *Volcano Deformation and Modeling on Active Volcanoes in the Philippines From ALOS InSAR Time Series*. ESA Special Publication, p. 74.
- Natvik, L.-J., Evensen, G., 2003. Assimilation of ocean colour data into a biochemical model of the North Atlantic: part 1. Data assimilation experiments. *J. Mar. Syst. The Use of Data Assimilation in Coupled Hydrodynamic, Ecological and Bio-geo-chemical Models of the Ocean. Selected Papers From the 33rd International Liege Colloquium on Ocean Dynamics, Held in Liege, Belgium on May 7–11th, 2001.* 40–41: pp. 127–153. [http://dx.doi.org/10.1016/S0924-7963\(03\)00016-2](http://dx.doi.org/10.1016/S0924-7963(03)00016-2).
- Newman, A.V., Dixon, T.H., Gourmelen, N., 2006. A four-dimensional viscoelastic deformation model for Long Valley Caldera, California, between 1995 and 2000. *J. Volcanol. Geotherm. Res.* 150:244–269. <http://dx.doi.org/10.1016/j.jvolgeores.2005.07.017>.
- Newman, A.V., Stiros, S., Feng, L., Psimoulis, P., Moschas, F., Saltogianni, V., Jiang, Y., Papazachos, C., Panagiotopoulos, D., Karagianni, E., Vamvakaris, D., 2012. Recent geodetic unrest at Santorini Caldera, Greece. *Geophys. Res. Lett.* 39, L06309. <http://dx.doi.org/10.1029/2012GL051286>.
- Nooner, S.L., Chadwick, W.W., 2009. Volcanic inflation measured in the caldera of Axial Seamount: implications for magma supply and future eruptions. *Geochim. Geophys. Res.* 10, Q02002. <http://dx.doi.org/10.1029/2008GC002315>.
- Papoutsis, I., Papanikolaou, X., Floyd, M., Ji, K.H., Kontoes, C., Paradissis, D., Zacharis, V., 2013. Mapping inflation at Santorini volcano, Greece, using GPS and InSAR. *Geophys. Res. Lett.* 40, 267–272.
- Parks, M.M., Moore, J.D.P., Papanikolaou, X., Biggs, J., Mather, T.A., Pyle, D.M., Raptakis, C., Paradissis, D., Hooper, A., Parsons, B., Nomikou, P., 2015. From quiescence to unrest: 20 years of satellite geodetic measurements at Santorini volcano, Greece. *J. Geophys. Res. Solid Earth* 120:1309–1328. <http://dx.doi.org/10.1002/2014JB011540>.
- Pinel, V., Poland, M.P., Hooper, A., 2014. Volcanology: lessons learned from synthetic aperture radar imagery. *J. Volcanol. Geotherm. Res.* 289:81–113. <http://dx.doi.org/10.1016/j.jvolgeores.2014.10.010>.
- Rivet, D., Brenguier, F., Clarke, D., Shapiro, N.M., Peltier, A., 2014. Long-term dynamics of Piton de la Fournaise volcano from 13 years of seismic velocity change measurements and GPS observations. *J. Geophys. Res. Solid Earth* 119:7654–7666. <http://dx.doi.org/10.1002/2014JB011307>.
- Ronchin, E., Masterlark, T., Molist, J.M., Saunders, S., Tao, W., 2013. Solid modeling techniques to build 3D finite element models of volcanic systems: an example from the Rabaul Caldera system, Papua New Guinea. *Comput. Geosci.* 52:325–333. <http://dx.doi.org/10.1016/j.cageo.2012.09.025>.
- Schmidt, S.F., 1966. Application of state-space methods to navigation problems. In: Leondes, C.T. (Ed.), *Advances in Control Systems*. Elsevier, pp. 293–340.
- Seiler, A., Evensen, G., Skjervheim, J.-A., Hove, J., Vabø, J.G., 2010. Using the ensemble Kalman filter for history matching and uncertainty quantification of complex reservoir models. In: Biegler, L., Biros, G., Ghattas, O., Heinkenschloss, M., Keyes, D., Mallick, B., Marzouk, Y., Tenorio, L., van Bloemen Waanders, B., Willcox, K. (Eds.), *Large-scale Inverse Problems and Quantification of Uncertainty*. John Wiley & Sons, Ltd., Chichester, UK, pp. 247–271.
- Sigmundsson, F., Durand, P., Massonnet, D., 1999. Opening of an eruptive fissure and seaward displacement at Piton de la Fournaise volcano measured by RADARSAT satellite radar interferometry. *Geophys. Res. Lett.* 26, 533–536.
- de Silva, S.L., Gregg, P.M., 2014. Thermomechanical feedbacks in magmatic systems: implications for growth, longevity, and evolution of large caldera-forming magma reservoirs and their supereruptions. *J. Volcanol. Geotherm. Res.* 282:77–91. <http://dx.doi.org/10.1016/j.jvolgeores.2014.06.001>.
- Simakin, A.G., Ghassemi, A., 2010. The role of magma chamber-fault interaction in caldera forming eruptions. *Bull. Volcanol.* 72:85–101. <http://dx.doi.org/10.1007/s00445-009-0306-6>.
- Skjervheim, J.-A., Evensen, G., Aanonsen, S.I., Ruud, B.O., Johansen, T.-A., 2007. Incorporating 4D seismic data in reservoir simulation models using ensemble Kalman filter. *SPE J.* 12:282–292. <http://dx.doi.org/10.2118/95789-PA>.
- Stankiewicz, J., Ryberg, T., Haberland, C., Fauzi, Natawidjaja, D., 2010. Lake Toba volcano magma chamber imaged by ambient seismic noise tomography: Lake Toba volcano magma chamber. *Geophys. Res. Lett.* 37. <http://dx.doi.org/10.1029/2010GL044211> (n/a–n/a).
- Williams, S.D.P., Bock, Y., Fang, P., Jamason, P., Nikolaidis, R.M., Prawirodirdjo, L., Miller, M., Johnson, D.J., 2004. Error analysis of continuous GPS position time series. *J. Geophys. Res. Solid Earth* 109, B03412. <http://dx.doi.org/10.1029/2003JB002741>.
- Wilson, G.W., Öezkan-Haller, H.T., Holman, R.A., 2010. Data assimilation and bathymetric inversion in a two-dimensional horizontal surf zone model. *J. Geophys. Res. Oceans* 115, C12057. <http://dx.doi.org/10.1029/2010JC006286>.
- Wilson, G., Öezkan-Haller, H.T., 2012. Ensemble-based data assimilation for estimation of river depths. *J. Atmos. Ocean. Technol.* 29:1558–1568. <http://dx.doi.org/10.1175/JTECH-D-12-00014.1>.
- Wilson, G.W., Öezkan-Haller, H.T., Holman, R.A., Haller, M.C., Honegger, D.A., Chickadel, C.C., 2014. Surf zone bathymetry and circulation predictions via data assimilation of remote sensing observations. *J. Geophys. Res. Oceans* 119:1993–2016. <http://dx.doi.org/10.1002/2013JC009213>.
- Zhang, J., Bock, Y., Johnson, H., Fang, P., Williams, S., Genrich, J., Wdowinski, S., Behr, J., 1997. Southern California permanent GPS geodetic array: error analysis of daily position estimates and site velocities. *J. Geophys. Res. Solid Earth* 102:18035–18055. <http://dx.doi.org/10.1029/97JB01380>.